Underdense plasma lens with a transverse density gradient

C. E. Doss,[1,*] R. Ariniello,[2] J. R. Cary,[1,3] S. Corde,[4] H. Ekerfelt,[2] E. Gerstmayr,[2] S. J. Gessner,[2] M. Gilljohann,[4] C. Hansel,[1] B. Hidding,[5,6] M. J. Hogan,[2] A. Knetsch,[4] V. Lee,[1] K. Marsh,[7] B. O'Shea,[2] P. San Miguel Claveria,[4] D. Storey,[2] A. Sutherland,[5,6] C. Zhang,[7] and M. D. Litos[1]

[1]*Center for Integrated Plasma Studies, Department of Physics, University of Colorado Boulder, Boulder, Colorado 80309, USA*
[2]*SLAC National Accelerator Laboratory, Menlo Park, California 94025, USA*
[3]*Tech-X Corporation, Boulder, Colorado 80301, USA*
[4]*LOA, ENSTA Paris, CNRS, Ecole Polychnique, Institut Polytechnique de Paris, 91762 Palaiseau, France*
[5]*Scottish Universities Physics Alliance, Department of Physics, University of Strathclyde, Glasgow G4 0NG, United Kingdom*
[6]*Cockcroft Institute, Sci-Tech Daresbury, Keckwick Lane, Daresbury, Cheshire WA4 4AD, United Kingdom*
[7]*University of California Los Angeles, Department of Electrical Engineering, Los Angeles, California 90095, USA*

(Received 21 December 2022; accepted 6 March 2023; published 30 March 2023)

We explore the implications of a transverse density gradient on the performance of an underdense plasma lens and nonlinear plasma-based accelerator. Transverse density gradients are unavoidable in plasma sources formed in the outflow of standard gas jets, which are used heavily in plasma accelerator communities. These density gradients lead to longitudinal variations in the transverse wakefields, which can transversely deflect an electron beam within the blowout wake. We present a theoretical model of the fields within the plasma blowout cavity based on empirical analysis of 3D particle-in-cell (PIC) simulations. Using this model, the transverse beam dynamics may be studied analytically, allowing for an estimation of the net kick of a witness electron bunch from an underdense plasma lens and for density uniformity tolerance studies in plasma accelerators and plasma lenses. This model is compared to PIC simulations with a single electron bunch and constant density profile, and to PIC simulations with two bunches and a thin, underdense plasma lens density profile with density ramps.

DOI: 10.1103/PhysRevAccelBeams.26.031302

I. INTRODUCTION

As the demand for higher energies and smaller spot sizes in electron accelerators has increased, interest has grown in novel accelerator technologies with greater focusing strength than conventional quadrupole magnets. One such example is the plasma lens, which is capable of focusing electron beams with field strengths orders of magnitude larger than conventional focusing magnets [1,2]. The general idea of a plasma-based focusing optic is well known and variations on the concept have been proposed and studied, such as the active plasma lens [3,4] and the overdense passive plasma lens [5–7]. Here, we focus on the underdense passive plasma lens, which can deliver strong, axisymmetric, linear focusing [8–10].

We consider an underdense passive plasma lens implemented by laser ionization of a gas jet outflow, such as in Refs. [11–13]. A femtosecond laser pulse is capable of ionizing a region of plasma localized within the outflow of a gas jet [14]. If the laser focus is much smaller than the gas outflow volume, the shape of the plasma lens will be characterized by the laser parameters and focusing optics. Within this region of ionized gas, for a typical gas jet outflow, the density profile would exhibit some degree of nonuniformity. A sketch of the hypothetical experimental layout we are considering is presented in Fig. 1. Transverse density gradients have been explored previously in the linear plasma wake regime as a pathway to a plasma-based undulator [15], but in this study, we concentrate on the nonlinear blowout regime.

An electron beam in the blowout wake of such a plasma lens will have a longitudinally varying deflection along the gas jet outflow axis that scales with the magnitude of the

*Christopher.Doss@Colorado.edu

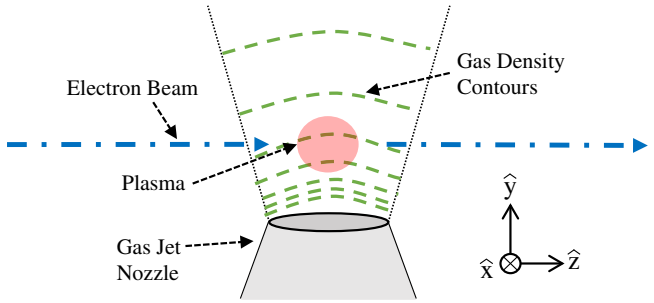

FIG. 1. Sketch of gas jet, plasma (red region), and electron beam (dashed blue) layout. Gas jet outflow (dashed green) is upwards in the y direction with an exponential density function. The outflow in the radial, x-z plane has a smoother Gaussian profile. The preformed plasma is ionized within a smaller region of this gas jet outflow by a laser propagating in the x direction (not shown). The electron beam propagates left to right in the z direction.

plasma density gradient. Though there may be useful ways to exploit this behavior, in general, it is likely to produce uncorrectable aberrations in the focusing of the electron beam. It is therefore important to be able to model and understand this behavior in order to sufficiently mitigate it when designing a plasma lens.

A typical density profile for a gas jet outflow can be described by a steep exponential or Lorentzian axial descent and a more gradual Gaussian or flattop profile in the outward radial dimension [16,17]. Here, using typical spatial coordinates for an electron beam propagating in the z direction, we assume the gas flow is directed vertically in the y direction and diffuses radially outward in the x-z plane. If we consider a gas number density of 5×10^{16} cm^{-3} just above the nozzle, the corresponding plasma wavelength is 149 μm, which sets the transverse scale of the plasma wake. In comparison, Ref. [16] measured the characteristic length scale of gas jet density variation to be larger than 550 μm in the vertical, outflow axis. The radial, Gaussian length scale is also larger than the plasma wavelength, and for a plasma centered within the gas jet outflow, the density gradient in this x-z plane is negligible. While this gas jet profile was measured in a high-density gas jet, gas jet outflows at lower densities can be measured using the technique described in Ref. [18]. Thus, the vertical, axial density profile can be approximated as varying linearly across the wake and the radial density profile can be assumed constant across the wake.

We quantify the transverse density gradient with the dimensionless parameter

$$g \equiv \left(\frac{\partial n}{\partial y}\right)\frac{c}{\omega_{pe} n_0}, \tag{1}$$

where c/ω_{pe} is the plasma skin depth, n_0 is unperturbed plasma number density at the height of the blowout center (defined as the drive beam axis) $y = 0$, and $\partial n/\partial y$ is the density gradient at $y = 0$ and is considered to be explicitly constant for the remainder of this work. Equation (1) quantifies the relative change in plasma density across the plasma skin depth.

For sufficiently small gradients where $g \ll 1$, we assume that the effects of the nonuniform plasma density are perturbative and the shape of the blowout wake retains its circular transverse cross section. We will revisit the region of validity for this assumption later in Sec. II. The density profile of the ion column is then given by

$$n_p(y) = n_0 + \left(\frac{\partial n}{\partial y}\right) y \tag{2}$$

over a circular cross section of blowout radius R, $x^2 + y^2 < R^2$. In this paper, we assume $\partial n/\partial y < 0$ to reflect a typical experimental setup where the gas jet is located below the electron beamline, yielding higher density at lower values of y.

The organization of this paper is as follows: In Sec. II, we perform particle-in-cell (PIC) simulations with and without a linear plasma density gradient to observe the difference in collective effects of the plasma wake. Section III derives a semiempirical model for the perturbations resulting from the density gradient: additional terms in the ion column's wakefield, the transverse drifting of the blowout wake's centroid, and the density gradient in the electron sheath. Section IV compares two-bunch PIC simulations of a plasma lens and linear density gradient with the observed vertical deflection and longitudinal variation from models in Sec. III. Section V calculates the transverse variation of the longitudinal wakefields due to the longitudinal variation of the transverse wakefields. Overall conclusions and future studies are discussed in Sec. VI.

II. NUMERICAL PIC SIMULATIONS

We begin our analysis by running several 3D PIC simulations of the wake formation in a plasma with a density gradient using a single, relativistic electron driver bunch. These are compared to identical simulations with no density gradient to find a semiempirical model that describes the effect of the linear transverse density gradient. The PIC simulation software we use is VSim [19], and the different simulation parameters used are summarized in Table I. Common to all simulations, the drive beam emittance is $\epsilon_N = 3.2$ mm mrad, the drive beam energy is $E = 10$ GeV, and the energy spread of the drive beam is Gaussian with $\sigma_\delta = 1\%$. The drive beam bunch length and transverse size were sufficient to drive a nonlinear blowout wake in all cases (see Table I for exact values used). In these simulations, a moving window follows the drive beam as it propagates 5 mm in the plasma until the blowout wake stops evolving and reaches a steady state.

TABLE I. Single-bunch simulation parameters and results. The top subtable lists the relevant wake dimensions for the zero-gradient cases and the input parameters across all simulations of the same density. The bottom su-table lists the measured values of wake dimensions and perturbative magnitudes from simulations with a nonzero density gradient. Measured values are defined later in the text. All simulations have appropriate simulation size and grid scales, and drive beam parameters are chosen to produce blowout wakes in different densities. Simulation parameters constant across all runs are listed in the text.

n_0 (cm^{-3})	$R_{\max}$ (μm)	$\xi_{\max}$ (μm)	Q_{drive} (nC)	$\sigma_{z,\mathrm{drive}}$ (μm)	$\sigma_{r,\mathrm{drive}}$ (μm)	dx, dy, dz (μm)	L_x, L_y (μm)	L_z (μm)
1×10^{16}	91.91	160.4	2	32.0	7.2	1.23	400	498
2×10^{16}	76.15	112.2	2	20.8	7.2	1.20	400	352
1×10^{17}	48.83	68.0	2.5	15.6	5.9	0.5	190	191

n_0 (cm^{-3})	$\partial n/\partial y$ (cm^{-4})	g	R_+ (μm)	R_- (μm)	α	$\langle\partial n/\partial y\rangle_{sh}$ (cm^{-4})	$\langle E_{sh}/R_p^2\rangle (V/m^3)$
1×10^{16}	4×10^{17}	0.212	98.27	86.95	0.0346	$1.17\times10^{18}\pm1.43\times10^{17}$	$6.25\times10^{16}\pm1.03\times10^{16}$
2×10^{16}	2.5×10^{15}	0.0005	76.171	76.137	0.000104	$1.63\times10^{15}\pm1.88\times10^{15}$	$3.83\times10^{14}\pm1.48\times10^{14}$
2×10^{16}	2.5×10^{16}	0.005	76.24	76.07	0.00103	$7.42\times10^{16}\pm2.05\times10^{16}$	$4.43\times10^{15}\pm4.60\times10^{14}$
2×10^{16}	2×10^{17}	0.038	77.09	75.02	0.00793	$5.85\times10^{17}\pm6.79\times10^{16}$	$3.62\times10^{16}\pm3.24\times10^{15}$
2×10^{16}	8×10^{17}	0.150	80.42	72.58	0.0309	$2.40\times10^{18}\pm2.63\times10^{17}$	$1.38\times10^{17}\pm1.26\times10^{16}$
1×10^{17}	2×10^{18}	0.034	49.57	47.94	0.00994	$7.93\times10^{18}\pm1.37\times10^{18}$	$3.76\times10^{17}\pm3.87\times10^{16}$
1×10^{17}	4×10^{18}	0.067	50.49	47.21	0.0198	$1.60\times10^{19}\pm2.69\times10^{18}$	$7.45\times10^{17}\pm7.42\times10^{16}$

A quantitative analysis of the simulations is given later in Sec. III. In this section, we introduce two qualitative effects apparent from analyzing the plasma electron density and blowout sheath along the vertical (plasma density gradient) direction, shown in Fig. 2. The longitudinal coordinate along the drive beam axis ξ is given by $\xi = ct - z$. First, we note that the simulations show the wake sheath trajectories in regions of plasma with higher (lower) density than n_0 behave as if the plasma skin depth is smaller (larger), as expected. The sheath in the lower density region will be longer and have a wider blowout radius than the sheath in the higher density region. While the cross-sectional shape of the rear of the wake is significantly altered by this dynamic, the bulk of the wake remains relatively circular. We can approximate longitudinal slices along the bulk of the blowout as having a circular transverse cross section with the center offset toward the lower density region. The magnitude of this offset grows along the length of the wake and, as a result, modifies the wakefield along the electron drive beam axis.

Second, a closer look at the blowout electron sheath reveals a linear, vertical density and axial current gradient with a separate magnitude than that of the unperturbed neutral plasma (Fig. 3). Here, as in Ref. [20], we consider the combined contribution of the electron charge density and axial (with respect to drive beam propagation axis) current as the full electron sheath profile:

$$n_{sh} = -(\rho - J_z/c)/e. \tag{3}$$

The result of this nonaxisymmetric electron sheath distribution contributes to the vertical component of the transverse wakefield within the blowout wake. However, toward the rear of the wake, the vertical sheath dependence becomes much steeper than in the center of the wake and, in cases with a higher plasma density gradient, the sheath profile can develop a quadratic or exponential form.

III. ANALYTIC AND EMPIRICAL MODELING

The most significant contribution to the transverse wakefield within the nonlinear blowout wake comes from the stationary, positively charged ions. While the transverse wakefield due to a uniform density ion column is linear and axisymmetric, the presence of the linear ion density gradient breaks this symmetry. To reach an analytic solution for the wakefield from an ion column described by Eq. (2), we first assume that the blowout itself is circular with radius R_p. The simulations presented in Sec. II show that this is a valid assumption everywhere except the rear-most region of the wake.

Under the assumption that the ion column is circular for a given longitudinal slice, we find a solution to the 2D Poisson-like equation [20] which gives the following form for the potential:

$$\psi = -\pi e n_0\{x^2 + [y - 2\bar{Y}(\xi)]^2\} - \frac{1}{2}\pi e\frac{\partial n}{\partial y}(y^3 + x^2 y). \tag{4}$$

Here, e is the fundamental electric charge and

$$\bar{Y}(\xi) = \frac{1}{4}\frac{R(\xi)^2}{n_0}\frac{\partial n}{\partial y} \tag{5}$$

is the "center of charge" for an ion column with a linear gradient in charge density. Because the blowout radius $R(\xi)$ has a longitudinal dependence, the transverse wakefields will correspondingly have a longitudinal

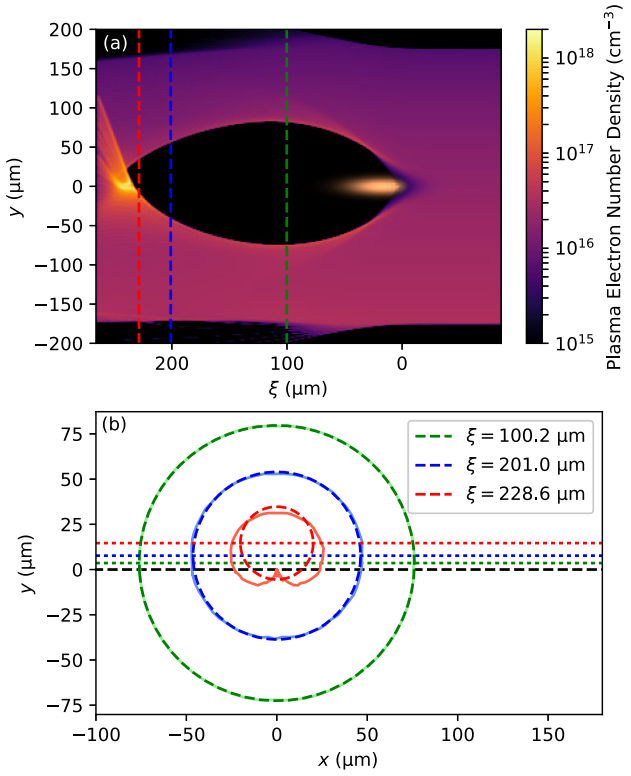

FIG. 2. PIC simulation of a nonlinear blowout wake driven by a single electron bunch with plasma density $n_0 = 2 \times 10^{16}$ cm^{-3} and a linear, vertical density gradient of $g = 0.150$. Subplot (a) shows a slice in the longitudinal-vertical plane, with the drive beam propagating toward the right. The colorbar represents the plasma electron density, and the drive beam is plotted with an arbitrary colorbar. The ions are assumed to form a stationary background with a number density given by Eq. (2). The three dashed lines mark the longitudinal positions that are examined in subplot (b), which plots the blowout wake's transverse cross section. The solid lines are the wake boundary from the simulation and the dashed lines are circular fits to the boundary. The dotted lines mark the wake's vertical center in each of the three circular fits. The black dashed line marks $y = 0$. The wake's centroid shifts upwards toward lower densities near the rear of the blowout while the cross section becomes less circular.

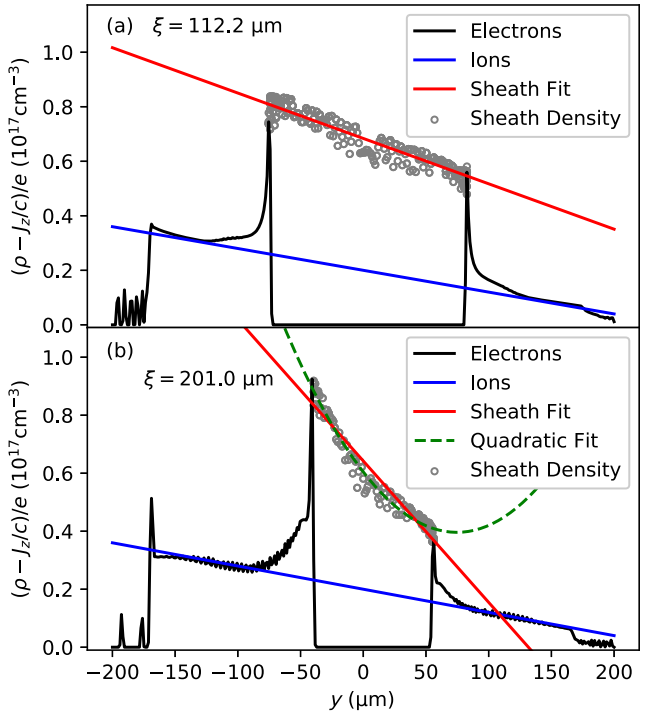

FIG. 3. Sum of plasma electron density and axial current (solid black) along y at $x = 0$. Subplots (a) and (b) are at longitudinal positions $\xi = 112.2$ μm and $\xi = 201.0$ μm, respectively. The density and gradient in this simulation are $n_0 = 2 \times 10^{16}$ cm^{-3} and $g = 0.150$. The initial plasma density before the arrival of the beam is shown in blue, which is also the density of the stationary ions. The projection of the electron sheath's peak for all x onto the y axis is shown by the gray circles, which represent the wake boundary for a given longitudinal slice. Linear fits to the peak sheath density across y are shown in solid red. In subplot (b), toward the back of the wake, the sheath density profile is not modeled perfectly by a linear function, and a sample quadratic fit is shown in dashed green.

variation. We look at the effects of this longitudinal variation later in this section.

Using Eq. (4), the transverse wakefields from the ions are calculated as $W_{x,y} = -\nabla_{x,y}\psi$:

$$W_x = 2\pi e n_0 x + \pi e \frac{\partial n}{\partial y}(xy) \tag{6}$$

and

$$W_y = 2\pi e n_0 [y - 2\bar{Y}(\xi)] + \frac{1}{2}\pi e \frac{\partial n}{\partial y}(3y^2 + x^2). \tag{7}$$

There are two notable features in Eqs. (4)–(7): first, the $-2\bar{Y}$ term in Eq. (7) indicates a transverse offset of the center of the linear focusing term toward the higher density side of the ion column. The second feature is the sextupole-like rightmost term in Eq. (4). The $x - y$ plane has the same y^3 dependence that produces a y^2-dependent focusing force of a sextupole magnet [21]. Interestingly, when compared to a sextupole magnet, the plasma lens is significantly less sensitive to beam centroid misalignment in the perpendicular x axis, but just as sensitive in the y axis. This feature, along with the compact size and high degree of tunability of the underdense plasma lens, may make it an attractive alternative to sextupole magnets for correcting higher order features in electron beams. However, it could prove difficult to access these fields since the strength of the sextupole fields is tied to the strength of the ion column's coincident focusing fields, as well as the vertical offset of the blowout center.

The effect of the fields expressed in Eqs. (6) and (7) contributes most significantly to the transverse field inside the blowout wake, but there remain two outstanding

features that lead to perturbations of the transverse wakefield: the vertical shifting of the blowout wake's centroid and the asymmetric electron sheath density and current profiles. These effects are far more difficult to describe analytically, so we have adopted simulation-based empirical methods to predict their effects.

First, we model the vertical drifting of the geometric wake center. This drift is due to the relatively weaker (stronger) restorative force on the plasma electrons from the ion column on the lower (higher) density side of the plasma. The imbalance causes the sheath to close more slowly (quickly) on the lower (higher) density side, shifting the transverse geometric center of each longitudinal slice of the blowout wake more to the lower density side from the front to the rear. In subplot (a) of Fig. 4, the sheath profiles of the lower and higher density sides of the wake are plotted and labeled as "greater" and "lesser," respectively. For the bulk of the wake, the geometric center drift is close to a linear function with respect to the longitudinal position within the blowout wake (Fig. 4).

We start by defining R_+ and R_- as the maximum radius of the greater and lesser sheaths, respectively. An empirical model that agrees well with the simulations in Sec. II is that R_+ and R_- are given by

$$R_\pm \approx R_{\max}\sqrt{1 \pm \left|\frac{\partial n}{\partial y}\right|\frac{R_{\max}}{n_0}A}; \qquad A \equiv 0.311, \tag{8}$$

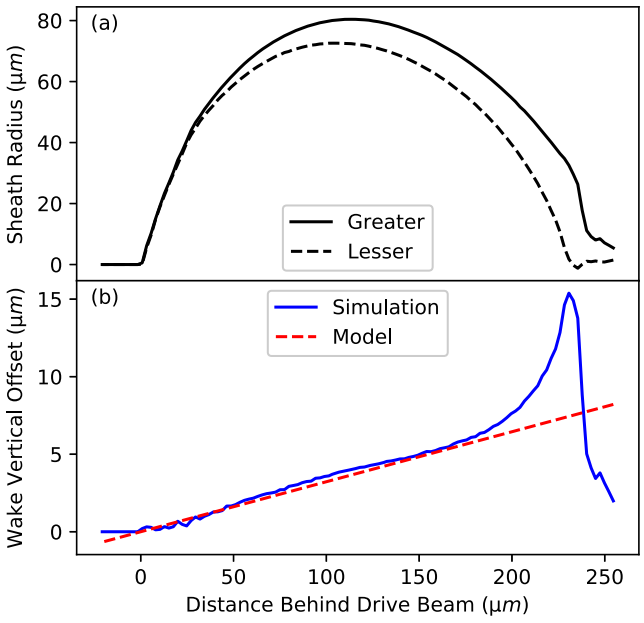

FIG. 4. Longitudinal evolution of the blowout wake's geometry and its sheath. In subplot (a), the greater and lesser curves refer to the sheath trajectories in the lower and higher density regions, respectively. In (b), the wake's centroid from a circular fit is plotted against the empirical model from Eq. (9). The model accurately predicts the wake's vertical offset everywhere except in the rear of the wake.

where $R_{\max}$ is the maximum blowout radius in a uniform plasma density n_0 and A is an empirical constant. The square root dependence is motivated by the scaling of the wake size with plasma wavelength [20]. Assuming the offset of the geometric wake center is 0 at the front, grows linearly, and is $(R_+ - R_-)/2$ at the location of $R_{\max}$; the wake center is given by

$$y_c(\xi) \approx -\mathrm{sgn}\left(\frac{\partial n}{\partial y}\right)\frac{(R_+ - R_-)}{2\xi_{\max}}\xi \equiv -\alpha\xi \tag{9}$$

where $\xi_{\max}$ is the longitudinal position of $R_{\max}$ and the scalar α is the slope of this vertical offset shift. Equation (9) is designed to have the opposite sign of $\partial n/\partial y$. As shown in Fig. 5, the empirical constant A is found by fitting this model to the measured center offset growth across all of the simulations (Table I) in the longitudinal region

$$\frac{1}{2}\xi_{\max} < \xi < \frac{3}{2}\xi_{\max} \tag{10}$$

where the growth is linear, as demonstrated in Fig. 4.

This offset of the wake center modifies our previous equations slightly, assuming that we want to keep the origin anchored to the drive beam axis. The y coordinate must now be expressed as $y - y_c(\xi)$, giving the following expressions for the transverse wakefields inside the wake:

$$W_x = 2\pi e n_c(\xi)x + \pi e\frac{\partial n}{\partial y}(x[y - y_c(\xi)]) \tag{11}$$

and

$$W_y = 2\pi e n_c(\xi)[y - y_c(\xi) - 2\bar{Y}(\xi)] + \frac{1}{2}\pi e\frac{\partial n}{\partial y}(3[y - y_c(\xi)]^2 + x^2), \tag{12}$$

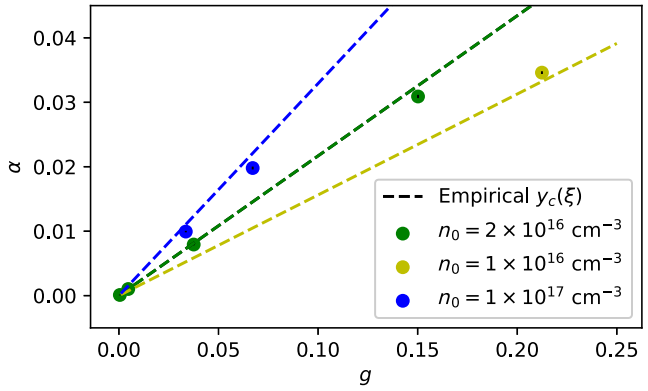

FIG. 5. Comparison of vertical offset growth along ξ observed in simulations (dots) with the theoretical prediction of Eqs. (8) and (9) (dashed lines). The simulations are grouped according to central density n_0, as $R_{\max}$ and $\xi_{\max}$ both depend on n_0.

with the density at the geometric center of a given longitudinal slice given by

$$n_c(\xi) = n_0 + \left(\frac{\partial n}{\partial y}\right) y_c(\xi). \tag{13}$$

Next, we investigate the vertical gradient of the electron sheath's peak density. Here we combine the contributions of the electron sheath's density and axial current using n_{sh}. Figure 3(a) shows that the peak of this combined electron sheath density and axial current has a linear dependence along the y dimension in the central region of the wake. This feature appears consistently in all the simulations in Sec. II, except at the rear of the wake. Here we use a simple model of the electron sheath as a hollow tube of charge with a density profile given by

$$n_{sh}(x, y) = n_{0,sh} + \left(\frac{\partial n}{\partial y}\right)_{sh} y, \tag{14}$$

where $n_{0,sh}$ is the combined sheath density and current at $y = 0$ and $(\partial n/\partial y)_{sh}$ is the gradient of the combined sheath density and current. This sheath profile is defined over the region

$$R(\xi)^2 < x^2 + [y - y_c(\xi)]^2 < [R(\xi) + L_{sh}(\xi)]^2, \tag{15}$$

where $R(\xi)$ is the local wake radius and $L_{sh}(\xi)$ is the sheath thickness, which we approximate as

$$L_{sh}(\xi) \approx CR(\xi); \qquad C \equiv 0.0904 \tag{16}$$

with C as an empirical constant. The transverse wakefield within such a structure is fairly uniform, especially near the center, so we approximate the sheath's transverse wakefield everywhere as equivalent to the value at the center of this simplified charge distribution:

$$W_{y,sh}(\xi) \approx -2\pi eCR^2(\xi)\left[\left(\frac{\partial n}{\partial y}\right)_i - \left(\frac{\partial n}{\partial y}\right)_{sh}\right]. \tag{17}$$

Here, $(\partial n/\partial y)_i$ is the density gradient of the ions from Eq. (2). In addition to the longitudinally varying wake radius $R(\xi)$ present in the other terms, Eq. (17) relies on empirical models for L_{sh} and $(\partial n/\partial y)_{sh}$. In the simulations performed in Sec. II, the sheath density gradient is fairly uniform over the bulk of the wake. We take the average linear fit of the sheath gradient over the longitudinal region $(1/2)\xi_{\max} < \xi < (3/2)\xi_{\max}$ and fit a linear relation using the ion density gradient to find

$$\left(\frac{\partial n}{\partial y}\right)_{sh} \approx B\left(\frac{\partial n}{\partial y}\right)_i; \qquad B \equiv 3.19 \tag{18}$$

with empirical constant B.

We make the assumption here that the transverse wakefields within the blowout are entirely defined by the contributions from the ion column and from the combined sheath density and current asymmetry. Therefore, after calculating the analytic wakefields from the ions using Eq. (12), we assume the difference between Eq. (12) and the wakefields in simulation is entirely from the sheath contribution of Eq. (17). The empirical constants B and C are found first by taking the representative average of $(\partial n/\partial y)_{sh}$ and $W_{y,sh}/R(\xi)^2$ in the region $(1/2)\xi_{\max} < \xi < (3/2)\xi_{\max}$ for all simulations in Table I. To account for numerical noise in the simulation, $(\partial n/\partial y)_{sh}$ and $W_{y,sh}/R(\xi)^2$ are smoothed using an 11-cell moving average algorithm. Figure 6 shows an example where the average $(\partial n/\partial y)_{sh}$ and $W_{y,sh}/R(\xi)^2$ were calculated for a simulation with $n_0 = 2 \times 10^{16}$ cm^{-3} and $g = 0.150$. It is worth noting in Fig. 6 that $W_{y,sh}/R(\xi)^2$ still has longitudinal variation. This suggests that the sheath model in Eqs. (14) and (16) is too simplified, and perhaps a more rigorous

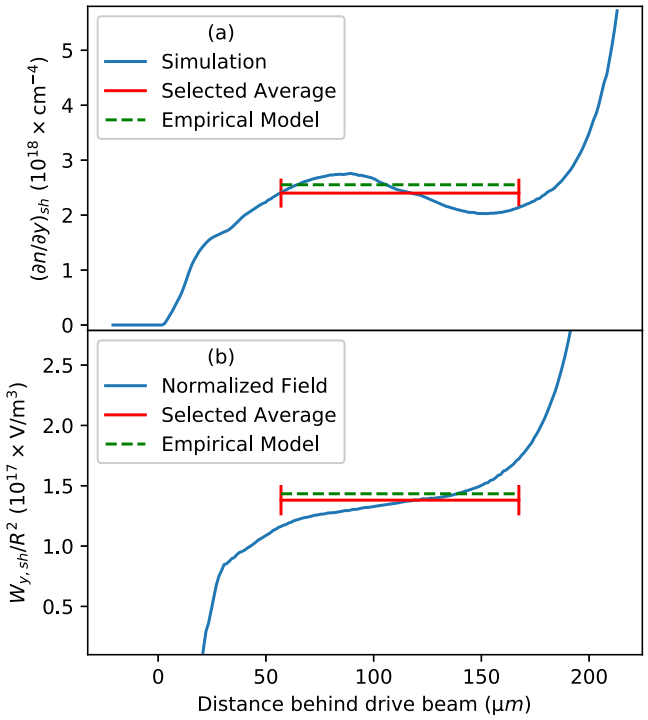

FIG. 6. Sheath density gradient (a) and sheath wakefield (b) plotted (blue) along the longitudinal length of the plasma wake with $n_0 = 2 \times 10^{16}$ cm^{-3} and $g = 0.150$. The sheath density gradient and sheath wakefield curves are smoothed using an 11-cell moving average algorithm to suppress the effects of simulation noise. The horizontal red lines represent the average value in the interval $(1/2)\xi_{\max} < \xi < (3/2)\xi_{\max}$ and the vertical red lines are twice the standard deviation. The dashed green lines represent the empirical models of Eqs. (18) (a) and (17) (b), which utilize the mean of the selected average values (red lines) taken from all of the simulations. After 150 μm, the model fails to accurately predict the density and field of the sheath.

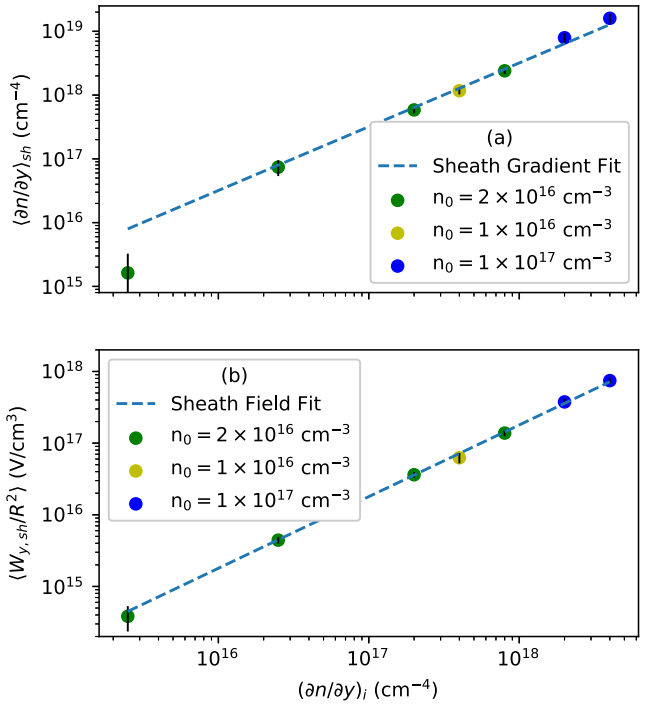

FIG. 7. Comparison between the empirical models of Eqs. (18) and (17) (dashed blue) with the averages taken for the sheath density gradient (a) and sheath wakefield (b) in the region $(1/2)\xi_{\max} < \xi < (3/2)\xi_{\max}$ across all simulations in Table I (dots). Error bars are the standard deviation of these quantities within this region.

model that includes longitudinal evolution of the sheath's shape, gradient, and thickness can describe the wakefields more accurately. The averages of $(\partial n/\partial y)_{sh}$ and $W_{y,sh}/R(\xi)^2$ are then plotted in Fig. 7, where the empirical constants B and C are found by fitting Eqs. (18) and (17) across all simulations in Table I on a logarithmic scale.

Including the sheath contribution, the vertical wakefield becomes

$$W_y = 2\pi e n_0(\xi)[y - y_c(\xi) - 2\bar{Y}(\xi)] + \frac{1}{2}\pi e \frac{\partial n}{\partial y}(3[y - y_c(\xi)]^2 + x^2) + W_{y,sh}(\xi). \quad (19)$$

The total transverse wakefields from Eqs. (11) and (19) are plotted in Fig. 8 at the middle of the wake $\xi = \xi_{\max}$, where $R(\xi_{\max}) = R_{\max}$. The wakefields from the simulation in Fig. 8 are calculated using the total transverse electric, $\vec{E}_{\perp,\text{full}}$, and magnetic, $\vec{B}_{\perp,\text{full}}$, fields present in the simulation, $\vec{W}_\perp = \vec{E}_{\perp,\text{full}} - c\vec{B}_{\perp,\text{full}} \times \hat{\xi}$ [20]. The transverse wakefield equations include several terms with longitudinal variation and the implication of this variation is discussed in the following section.

Toward the rear of the wake, the sheath density gradient becomes much steeper than what the model predicts, and in cases with a large plasma density gradient g, the vertical sheath density profile becomes more quadratic or exponential. For such a density profile, the corresponding wakefield is no longer constant and a slight asymmetric focusing/defocusing perturbation develops. This, along with the limited region where the vertical offset drift is linear, as seen in Fig. 4, may add difficulty in applying this model to PWFA applications, where often the location of a witness beam for optimal acceleration and loading is in the rear of the wake.

IV. LONGITUDINAL VARIATION OF TRANSVERSE WAKEFIELDS

To demonstrate the effectiveness of the preceding model, we consider the vertical deflection of a trailing witness bunch in an underdense, passive plasma lens, similar to that described in [10] but with a linear plasma density gradient. For such a lens, the witness bunch will have a longitudinally dependent vertical deflection predicted by Eq. (19). We perform another set of PIC simulations with both an electron drive bunch and a trailing witness bunch at various longitudinal separation distances. The central plasma density and density gradient are set at $n_0 = 2 \times 10^{16}$ cm^{-3} and $\partial n/\partial y = 8 \times 10^{17}$ cm^{-4}, with $g = 0.150$. The normalized gradient used here is larger than for a typical gas jet profile, but it is useful for a more pronounced demonstration of this theory. Cases with a smaller normalized gradient will have a smaller effect on the deflection, but the dependence of the deflection angle on the longitudinal position will be similar.

In addition to the inclusion of a witness bunch, a realistic model of the longitudinal plasma density profile is used, given by

$$n_p(x, y, \xi) = n_0 \left[\frac{1}{2} + \frac{1}{2}\tanh\left(\frac{\xi + a}{b}\right)\right] \times \left[\frac{1}{2} - \frac{1}{2}\tanh\left(\frac{\xi - a}{b}\right)\right]\left(1 + \frac{(\partial n/\partial y)}{n_0} y\right), \quad (20)$$

where $a = 150$ μm is the half width at half maximum (HWHM) and $b = 20$ μm determines the ramp steepness. This results in a plasma density profile with a flattop region of about 200 μm in length and density ramps with a full width of about 100 μm.

The drive beam, plasma, and grid size parameters in these two-bunch simulations are all equivalent to those used in the corresponding single-bunch simulations from Table I. The witness beam parameters are as follows: energy $\gamma_L m_e c^2 = 10$ GeV, Gaussian energy spread $\sigma_\delta = 0.1\%$, longitudinal bunch length $\sigma_z = 6.0$ μm, transverse bunch size $\sigma_r = 6.0$ μm, normalized emittance $\epsilon_N = 3.1$ mm mrad, and charge $Q = 0.5$ nC.

The vertical deflection angle of the witness beam for each drive-witness separation distance is plotted in Fig. 9. We compare the deflection measured in the two-bunch PIC

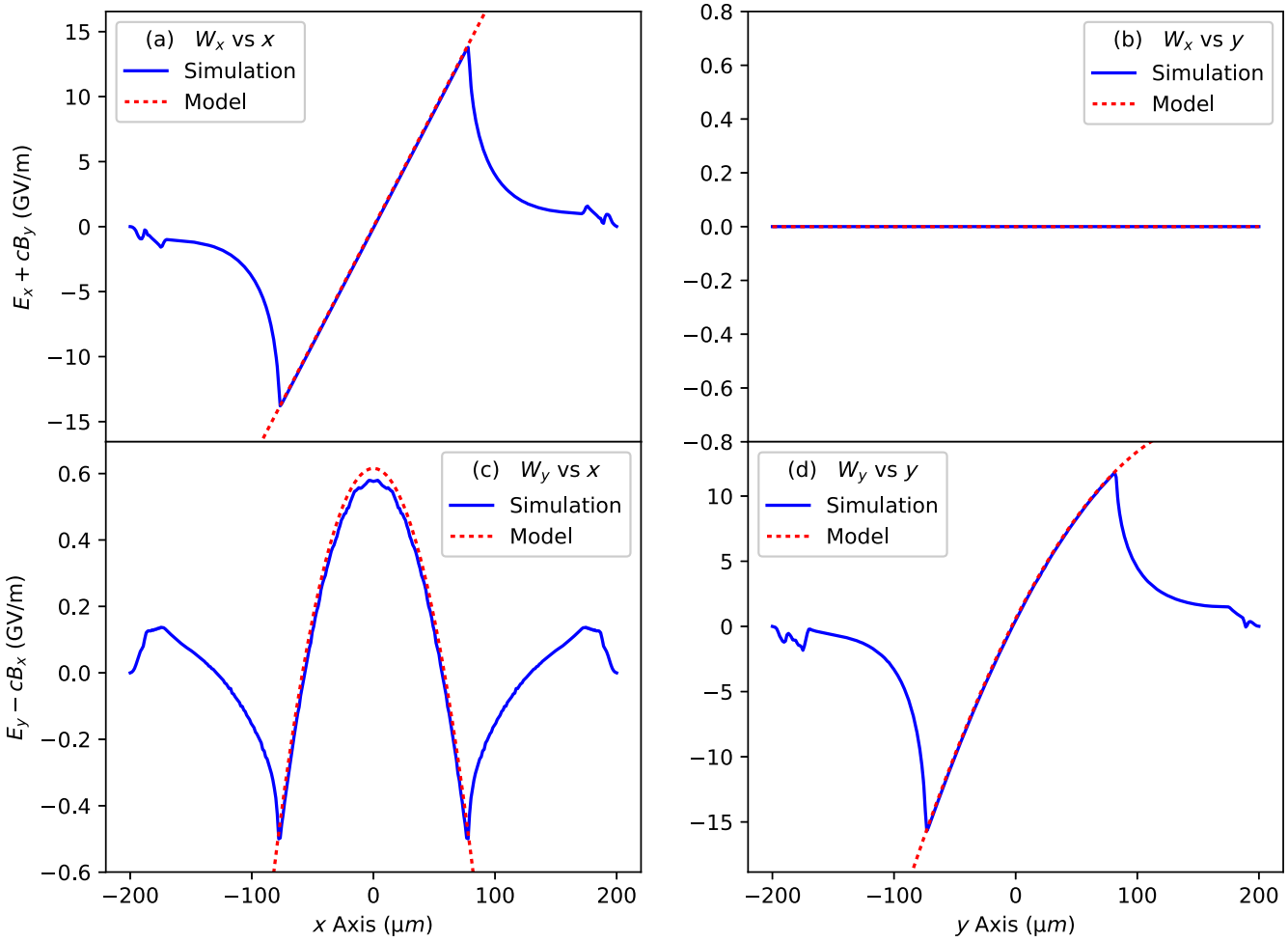

FIG. 8. Transverse electromagnetic fields along the principle axes from a simulation with a central density $n_p = 2 \times 10^{16}$ cm^{-3} and a normalized transverse gradient $g = 0.150$. (solid blue) and from the model derived in this work (dashed red). Subplot (a) shows a linear dependence on x for the horizontal focusing force; (b) shows zero variation of the horizontal focusing force along the y axis; (c) shows the vertical deflection and the small, nonlinear dependence on x of the vertical focusing force; and (d) shows the significant nonlinear dependence on y of the vertical focusing force.

simulations with the deflection predicted by Eq. (19) using $R(\xi)$ and $\xi_{\max}$ from the zero gradient, steady-state simulation at $n_0 = 2 \times 10^{16}$ cm^{-3}. The deflection angle is calculated with respect to the drive beam axis in the longitudinal-vertical plane as

$$\theta_{\text{def}} = \frac{-eL_{\text{lens}}}{\gamma_L m_e c^2} W_y|_{y=0} \tag{21}$$

with e the elementary charge, m_e the electron mass, and $L_{\text{lens}} = 300$ μm, the effective plasma lens thickness [10]. The deflection calculated from the electromagnetic fields of the single-bunch, long-propagation simulation from Sec. II with the same density and gradient is also plotted, assuming no density ramps. Here we consider this single-bunch simulation to be effectively steady state, as the wake has stopped evolving after 5 mm of propagation distance. The agreement between these plots is good throughout most of the wake, but we can make a few important observations from the discrepancies between them.

First, the difference between the empirical model and the steady-state fields arises from the breakdown of the assumptions in the empirical model toward the rear of the wake. With the high-density sheath approaching the drive beam axis more rapidly than the low density sheath, the blowout wake cross section begins to resemble more of a heart shape than a circle. We can interpret from Fig. 4 that this departure from a roughly circular cross section takes place beyond 200 μm behind the drive beam, at which point the model will no longer accurately reflect the fields of the ion column. However, in Fig. 9, the results diverge well before 200 μm, indicating this is not the primary source of error. Rather, in Fig. 6, we can see that the model for the sheath's wakefield is only valid in the center of the

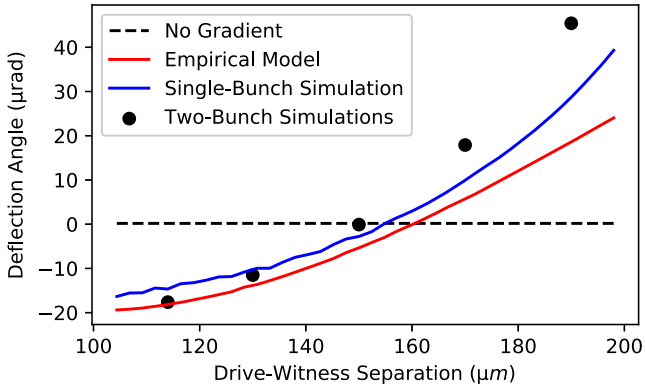

FIG. 9. The longitudinal variation of the net deflection angle (left axis) from an underdense plasma lens with FWHM = 300 μm, $n_0 = 2 \times 10^{16}$ cm^{-3}, and $g = 0.150$ for a witness beam behind and on the same axis of a drive beam. Solid red is the prediction from the empirical model in Eq. (19), solid blue is the prediction from the steady-state simulation of the same gradient and not including density ramps, and the black dots are taken from two-bunch simulations in a short plasma lens density profile. The maximum blowout radius in these simulations occurs at a distance $\xi_{\max} = 112.2$ μm behind the drive beam.

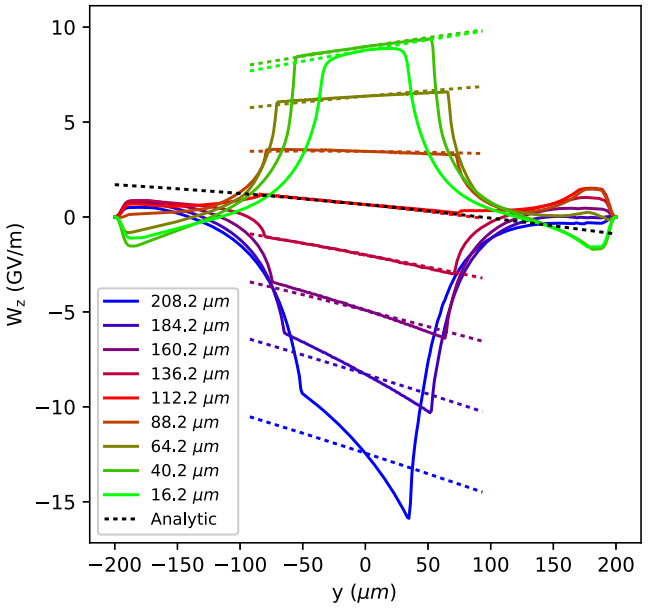

FIG. 10. Transverse variation of the longitudinal wakefield at various longitudinal positions in the blowout wake behind the drive beam. For example, the light green curve is 16.2 μm behind the center of the drive beam, and the dark blue curve is 208.2 μm behind the drive beam, close to the rear of the wake. Dashed lines of the corresponding color represent the calculated slope using Eqs. (23) and (24). The slope of this curve at the center of the wake ($\xi = 112.2$ μm) matches the analytic solution of Eq. (25) (dashed black).

wake and diverges around $\xi = 150$ μm because the density gradient of the electron sheath becomes much steeper than the model predicts.

Second, the difference between the single-bunch steady-state fields and the results of the two-bunch simulations is due to the longitudinal density profile used in the latter. With this density profile, the beams do not propagate long enough through the flattop region of the plasma to reach a steady-state plasma wake. The density ramps also contribute to these nonsteady-state conditions. We see significant variation in the instantaneous transverse wakefield that appears to oscillate about the expected steady-state transverse wakefield for the short duration of the plasma lens. Furthermore, it is possible that the transverse wakefield of the witness beam itself has enough of an effect on the sheath of the blowout that the rear of the witness beam is affected.

We here make a general observation from Eq. (19) that a witness beam located toward the middle or front of the wake will tend to experience an ion-dominated deflection toward the direction of the gas jet nozzle, while a witness beam near the rear of the wake will experience a sheath-dominated deflection away from the gas jet. This trend is clearly observable in Fig. 9.

V. TRANSVERSE VARIATION OF LONGITUDINAL WAKEFIELDS

Since there is a longitudinal variation of the transverse focusing fields in the blowout wake, the Panofsky-Wenzel theorem predicts a corresponding transverse variation of the longitudinal accelerating fields [22,23]. This is indeed what we observe in simulations as shown in Fig, 10, and we can calculate the slope of W_z using Eqs. (11) and (19) and solving

$$\frac{\partial W_z}{\partial x} = -\frac{\partial W_x}{\partial \xi}$$
$$\frac{\partial W_z}{\partial y} = -\frac{\partial W_y}{\partial \xi}. \tag{22}$$

We find the following expression for the longitudinal wakefield:

$$W_z = \frac{1}{2}\pi e \alpha \frac{\partial n}{\partial y}(x^2 - y^2) + \Omega_{\text{lin}} y + W_{z,0}(\xi), \tag{23}$$

where α is defined from Eq. (9) and $W_{z,0}(\xi)$ is the longitudinal wakefield along the drive beam axis, and Ω_{lin} is defined

$$\Omega_{\text{lin}} \equiv \pi e \left[\alpha^2 \frac{\partial n}{\partial y}\xi - 2n_0\alpha - \alpha\left(\frac{\partial n}{\partial y}\right)^2 \frac{R^2(\xi)}{n_0} + 2R(\xi)\frac{\partial n}{\partial y}\frac{\partial R(\xi)}{\partial \xi}\left(1 - \frac{\alpha}{n_0}\frac{\partial n}{\partial y}\xi\right) + 4CR(\xi)(1-B)\frac{\partial n}{\partial y}\frac{\partial R(\xi)}{\partial \xi}\right]. \tag{24}$$

The main contributions to a nonflat longitudinal wakefield are found in Eq. (24). In particular, the largest terms are the quantities $2n_0\alpha$ and $2R(\xi)(\partial n/\partial y)(\partial R(\xi)/\partial\xi)$. If we consider the middle of the wake ($\xi = \xi_{\max}$), the longitudinal evolution of the wake radius drops out of Eq. (24) and we find a much simpler expression:

$$\Omega_{\text{lin,mid}} = \pi e\alpha\left[\alpha\frac{\partial n}{\partial y}\xi_{\max} - 2n_0 - \left(\frac{\partial n}{\partial y}\right)^2\frac{R_{\max}^2}{n_0}\right]$$
$$\Omega_{\text{lin,mid}} \approx -2\pi e\alpha n_0. \tag{25}$$

Equation (23) agrees well with observations in the front of the wake. As with the vertical transverse wakefield, the longitudinal wakefield plots in Fig. 10 agree less with Eq. (23) toward the rear of the wake. We also note that the position in the wake that corresponds to a flat longitudinal wakefield is in the front half of the wake between 60 and 90 μm, approximately where the slope of the transverse wakefield would be zero in Fig. 9.

There is no point along the drive beam axis where both the transverse field is zero and the longitudinal field is uniform. However, these conditions can be satisfied at a transverse offset position in the wake. In this case, one would solve Eq. (24) to find ξ where the longitudinal wakefield slope is zero, then solve Eq. (19) to find the needed vertical offset from the drive beam axis to achieve zero deflection. This solution would be in the front half of the wake with a slight decelerating field, sufficient for a plasma lens. But in the context of a plasma accelerator that requires an accelerating field, it would be impossible to find a longitudinal position inside the wake with a transversely uniform accelerating field.

VI. DISCUSSION

In this paper, we investigated the effects of a linear density gradient on the field structure in a nonlinear plasma wake using PIC simulations to form a combined analytic and empirical model. The linear density gradient is a good approximation for the plasma profile produced in a gas jet outflow, as the length scales of the plasma wake are typically small compared to the characteristic length scales of the gas outflow. The variation of the fields in the plasma wake with respect to the uniform density case arises from the transverse density gradient of the ions and the sheath electrons, as well as the longitudinally drifting transverse center of the wake. This drifting of the wake's center is similar to what was seen when using an elongated, tilted drive beam [24]. A theoretical model of the field structure was derived based on an analytic approach supplemented with empirical models based on observations from PIC simulations.

The model presented here does not have an unlimited range of applicability. There are two constraints in particular that one should consider. First, the density gradient must be linear or very close to linear. This condition will likely be satisfied in the outflow of a typical gas jet so long as the blowout radius is small compared to the characteristic length scale of the gas jet's exponential density profile. Second, the plasma density must not fall to zero within the blowout radius, otherwise, the wake would deform into a noncircular shape early in the blowout. This implies that the normalized density gradient radius must satisfy the condition $gR_{\max}\omega_{pe}/c < 0.5$.

We applied this model to predict the net deflection of a witness beam in a two-bunch simulation propagating through a 400-μm thick plasma lens with a realistic density profile and an exaggerated density gradient compared to a realistic gas jet. The model worked well when the witness beam was located within the bulk of the plasma wake, diverging from the simulation results only when approaching the rear of the wake where our assumption of a circular cross section and a constant, linear sheath density gradient break down. Within the region $(1/2)\xi_{\max} < \xi < (3/2)\xi_{\max}$ where the electron sheath model was empirically obtained, the model agrees very well. Additional factors that limited the accuracy of this model were the density ramps and an overall length that was too short to allow a steady state to be reached.

The net deflection of the witness beam depends on its longitudinal location within the wake, and shifts from an ion-driven deflection toward the higher density side when near the front of the wake to a sheath-driven deflection toward the lower density side when near the rear of the wake. This model allows for the prediction of the correct position of the witness beam to prevent a net transverse deflection despite the presence of the transverse density gradient. Alternatively, one could design a plasma lens with a longitudinally varying central density n_0 that results in nonzero deflections throughout the plasma but a net-zero deflection overall.

In addition, this model describes the transverse dependence of the longitudinal wakefield in the wake. For a thin plasma lens, this is likely to be a negligible effect. However, this model applies equally well to a plasma wakefield accelerator operating in the nonlinear blowout regime, and in this context, the longitudinal field variation could be of great consequence. This model can predict the magnitude of this effect, which may be of critical importance when designing a plasma-based accelerator in an elongated gas jet that aims to preserve beam quality (e.g., emittance and energy spread), such as presented in Refs. [25,26].

While the primary focus of this study is electron beam-driven nonlinear blowout wakes, many of the same conclusions can be drawn for a high-intensity laser-driven wakes. An important caveat, however, is that the front of the laser driver will experience a transverse deflection due to the transverse gradient of the plasma refractive index [27]. Meanwhile, the behavior of an electron beam

driver would be somewhat more complex. The tail of the beam inside the blowout would oscillate about the center of the ion column's focusing force. This may, in turn, lead to an average drift of the wake center over time as the head of the beam erodes. The dynamics of the head of the beam, however, are difficult to model and predict with certainty without parameter-specific simulations.

It is worth noting that the effects of the transverse density gradient on the performance of a thin, underdense plasma lens may not always be of negative value. A particular asymmetric density profile can be designed as to make a plasma kicker, similar to what is discussed in Refs. [28,29]. A plasma kicker with a large normalized density gradient might find use as a compact replacement for a dipole magnet when integrating or separating drive and witness bunches in a multistage, plasma-based linear accelerator [30]. Under the correct conditions, it could even potentially be used as a compact alternative to a sextupole magnet for correcting beam aberrations with a more forgiving beam alignment tolerance. One could even design a plasma-based beam streaker that is capable of deflecting the head and tail of an electron beam at different angles, as evidenced in Fig. 9.

ACKNOWLEDGMENTS

This material is based upon work supported by the U.S. Department of Energy Office of Science (DOE-OOS), Office of High Energy Physics under Award No. DE-SC001796. This research used resources of the National Energy Research Scientific Computing Center, a DOE Office of Science User Facility supported by the Office of Science of the U.S. Department of Energy under Contract No. DE-AC02-05CH11231 using NERSC Grant No. HEP-ERCAP0024521.

[1] P. Chen, S. Rajagopalan, and J. Rosenzweig, Phys. Rev. D **40**, 923 (1989).

[2] P. Chen, K. Oide, A. M. Sessler, and S. S. Yu, Phys. Rev. Lett. **64**, 1231 (1990).

[3] J. van Tilborg, S. Steinke, C. G. R. Geddes, N. H. Matlis, B. H. Shaw, A. J. Gonsalves, J. V. Huijts, K. Nakamura, J. Daniels, C. B. Schroeder, C. Benedetti, E. Esarey, S. S. Bulanov, N. A. Bobrova, P. V. Sasorov, and W. P. Leemans, Phys. Rev. Lett. **115**, 184802 (2015).

[4] C. A. Lindstrøm, E. Adli, G. Boyle, R. Corsini, A. E. Dyson, W. Farabolini, S. M. Hooker, M. Meisel, J. Osterhoff, J.-H. Röckemann, L. Schaper, and K. N. Sjobak, Phys. Rev. Lett. **121**, 194801 (2018).

[5] H. Nakanishi, Y. Yoshida, T. Ueda, T. Kozawa, H. Shibata, K. Nakajima, T. Kurihara, N. Yugami, Y. Nishida, T. Kobayashi, A. Enomoto, T. Oogoe, H. Kobayashi, B. S. Newberger, S. Tagawa, K. Miya, and A. Ogata, Phys. Rev. Lett. **66**, 1870 (1991).

[6] G. Hairapetian, P. Davis, C. E. Clayton, C. Joshi, S. C. Hartman, C. Pellegrini, and T. Katsouleas, Phys. Rev. Lett. **72**, 2403 (1994).

[7] J. S. T. Ng, P. Chen, W. Craddock, F. J. Decker, R. C. Field, M. J. Hogan, R. Iverson, F. King, R. E. Kirby, T. Kotseroglou, P. Raimondi, D. Walz, H. A. Baldis, P. Bolton, D. Cline, Y. Fukui, V. Kumar, C. Crawford, R. Noble, K. Nakajima, A. Ogata, and A. W. Weidemann, arXiv:physics/0008138.

[8] N. Barov and J. B. Rosenzweig, Phys. Rev. E **49**, 4407 (1994).

[9] M. C. Thompson, H. Badakov, J. B. Rosenzweig, G. Travish, N. Barov, P. Piot, R. Fliller, G. M. Kazakevich, J. Santucci, J. Li, and R. Tikhoplav, Phys. Plasmas **17**, 073105 (2010).

[10] C. E. Doss, E. Adli, R. Ariniello, J. Cary, S. Corde, B. Hidding, M. J. Hogan, K. Hunt-Stone, C. Joshi, K. A. Marsh, J. B. Rosenzweig, N. Vafaei-Najafabadi, V. Yakimenko, and M. Litos, Phys. Rev. Accel. Beams **22**, 111001 (2019).

[11] R. Lehe, C. Thaury, E. Guillaume, A. Lifschitz, and V. Malka, Phys. Rev. ST Accel. Beams **17**, 121301 (2014).

[12] C. Thaury, E. Guillaume, A. Döpp, R. Lehe, A. Lifschitz, K. Ta Phuoc, J. Gautier, J.-P. Goddet, A. Tafzi, A. Flacco, F. Tissandier, S. Sebban, A. Rousse, and V. Malka, Nat. Commun. **6**, 6860 (2015).

[13] S. Kuschel, D. Hollatz, T. Heinemann, O. Karger, M. B. Schwab, D. Ullmann, A. Knetsch, A. Seidel, C. Rödel, M. Yeung, M. Leier, A. Blinne, H. Ding, T. Kurz, D. J. Corvan, A. Sävert, S. Karsch, M. C. Kaluza, B. Hidding, and M. Zepf, Phys. Rev. Accel. Beams **19**, 071301 (2016).

[14] M. V. Ammosov, N. B. Delone, and V. P. Kraĭnov, Sov. Phys. JETP **64**, 4 (1986), https://ui.adsabs.harvard.edu/abs/1986JETP...64.1191A/abstract.

[15] G. Stupakov, Phys. Plasmas **24**, 113110 (2017).

[16] A. Behjat, G. J. Tallents, and D. Neely, J. Phys. D **30**, 2872 (1997).

[17] S. Semushin and V. Malka, Rev. Sci. Instrum. **72**, 2961 (2001).

[18] C. Zhang, Z. Nie, Y. Wu, M. Sinclair, C.-K. Huang, K. A. Marsh, and C. Joshi, Plasma Phys. Controlled Fusion **63**, 095011 (2021).

[19] C. Nieter and J. R. Cary, J. Comput. Phys. **196**, 448 (2004).

[20] W. Lu, C. Huang, M. Zhou, W. B. Mori, and T. Katsouleas, Phys. Rev. Lett. **96**, 165002 (2006).

[21] S. Y. Lee, *Accelerator Physics (Fourth Edition)* (World Scientific Publishing Company, Singapore, 2018).

[22] W. K. H. Panofsky and W. A. Wenzel, Rev. Sci. Instrum. **27**, 967 (1956).

[23] S. Vaganian and H. Henke, Part. Accel. **48**, 239 (1995), https://cds.cern.ch/record/1108316/files/p239.pdf.

[24] E. Adli, S. Corde, R. J. England, J. Frederico, S. J. Gessner, S. Li, Z. Wu, M. J. Hogan, M. D. Litos, W. An, C. E. Clayton, K. A. Marsh, W. Lu, W. Mori, C. Joshi, N. Vafaei-Najafabadi, and P. Muggli, in *Proceedings of t he 3rd International Particle Accelerator Conference, New Orleans, LA, 2012* (IEEE, Piscataway, NJ, 2012), pp. 43–45.

[25] B. Miao, J. E. Shrock, L. Feder, R. C. Hollinger, J. Morrison, R. Nedbailo, A. Picksley, H. Song, S. Wang, J. J. Rocca, and H. M. Milchberg, Phys. Rev. X **12**, 031038 (2022).

[26] J. E. Shrock, B. Miao, L. Feder, and H. M. Milchberg, Phys. Plasmas **29**, 073101 (2022).
[27] Y. Ma, D. Seipt, S. J. D. Dann, M. J. V. Streeter, C. A. J. Palmer, L. Willingale, and A. G. R. Thomas, Phys. Plasmas **25**, 113105 (2018).
[28] P. Muggli, S. Lee, T. Katsouleas, R. Assmann, F. J. Decker, M. J. Hogan, R. Iverson, P. Raimondi, R. H. Siemann, D. Walz, B. Blue, C. E. Clayton, E. Dodd, R. A. Fonseca, R. Hemker, C. Joshi, K. A. Marsh, W. B. Mori, and S. Wang, Phys. Rev. ST Accel. Beams **4**, 091301 (2001).
[29] G. Wittig, O. Karger, A. Knetsch, Y. Xi, A. Deng, J. B. Rosenzweig, D. L. Bruhwiler, J. Smith, G. G. Manahan, Z.-M. Sheng, D. A. Jaroszynski, and B. Hidding, Phys. Rev. ST Accel. Beams **18**, 081304 (2015).
[30] C. A. Lindstrøm, Phys. Rev. Accel. Beams **24**, 014801 (2021).